Nanoscale

PAPER

View Article Online
View Journal

Cite this: DOI: 10.1039/d6nr00074f

Quantifying chiral handedness of core–shell inorganic nanotubes *via* electron microscopy and diffraction

Kaiyuan Wang, [a] Beilynn Geiss,[b] Roy Geiss,[a] James R. Neilson, [a] Alla Zak[c] and Justin B. Sambur *[a]

Intrinsically chiral inorganic nanotubes (NTs) based on WS_2 and MoS_2 are promising visible-light-absorbing materials for heterogeneous enantioselective photocatalysis and, potentially, for fundamental studies of the chirality-induced spin selectivity (CISS) effect. Accurate identification of chiral handedness is essential for advancing enantioselective applications of these materials, but existing imaging and diffraction-based protocols do not rapidly facilitate the identification of NT handedness. We present a combined transmission electron microscopy (TEM) and selected-area electron diffraction (SAED) approach for determining the chiral handedness of WS_2 NTs that contain WO_x cores. We observe the WO_x core lattice and WS_2 atomic layers in the same TEM image. By comparing the lattice orientations of the WO_x core relative to the WS_2 layers, and confirming the relationship with the chiral angle revealed by SAED patterns, we can unambiguously identify the right- or left-handed structure of individual NTs. In addition, we show that moiré patterns formed from the WS_2 shells and oxide core can also be used to characterize lattice orientation, chiral indices, and handedness. This approach requires no additional sample preparation, instrumentation, or experimental adjustments, and may be applied broadly to other core–shell nanotube systems such as MoS_2, BN, and carbon NTs. The significance of this work is that it enables reliable handedness determination of chiral core–shell nanostructures and addresses a key difficulty in the existing characterization methods of multiwalled NTs. We envision that the single particle catalysis community can leverage these methods to study the structure–activity relationships of this unique class of intrinsically chiral semiconductor nanostructures.

Received 7th January 2026,
Accepted 23rd March 2026

DOI: 10.1039/d6nr00074f

rsc.li/nanoscale

Introduction

Inorganic NTs are exciting materials that have been explored for applications in lubricants,[1] superconductors,[2] batteries,[3] photocatalysts,[4,5] and hydrogen storage.[6,7] NTs based on transition metal dichalcogenides (TMDs) such as MoS_2 and WS_2 are emerging as intriguing materials due to their inherently chiral surfaces,[8,9] which opens possibilities for a broad range of applications spanning spin-selective catalysis,[10–13] chiral molecule sensing,[14] and light–matter interactions.[15]

The central challenge in advancing inorganic NTs for enantioselective chemical synthesis applications is that current synthesis methods produce racemic mixtures with wide variations in diameter, wall thickness, chiral index, and handedness. WS_2 NTs grow from $W_{18}O_{49}$ nanowhiskers.[16–18] The high-temperature sulfurization of the $W_{18}O_{49}$ nanowhiskers yields an oxide core sheathed by a few closed layers of WS_2.[19] This process leads to a core–shell $W_{18}O_{49}$@WS_2 nanostructure, and the NT diameter and chirality depend on the heterogeneous size distribution of $W_{18}O_{49}$ nanowhiskers. This structural heterogeneity makes it difficult to connect the structure with function using conventional ensemble-averaged characterization tools. Moreover, oxide cores can influence catalysis[20] and may facilitate photogenerated charge-carrier separation at the core–shell interface, yet there are no established methods for characterizing the chiral structural properties of these core–shell architectures at the single-nanotube level, particularly the chiral handedness of each inorganic NT in the heterogeneous sample batch.

Several characterization approaches have been used to determine the chiral structural properties of single- and double-walled carbon NTs, each with advantages and disadvantages. Electron diffraction is a widely used approach to determine the chiral indices of Te nanocrystals[21] and carbon NTs,[22,23] but this approach does not directly reveal the chiral handedness (*i.e.*, right- or left-handed NT). Liu and Qin pro-

[a]*Department of Chemistry, Colorado State University, 1301 Center Ave, Chemistry B101, Fort Collins, Colorado, USA. E-mail: jsambur@colostate.edu*
[b]*Skidmore College, Saratoga Springs, New York, USA*
[c]*Department of Sciences, Holon Institute of Technology, 52 Golomb st., Holon, Israel*

posed a method using the principal line shift in the SAED pattern to determine the handedness of carbon NTs.[24] However, this approach relies on applying a mechanical force to twist an individual NT and then use changes in the SAED pattern to distinguish between left- and right-handed structures, which is challenging to implement experimentally. Atomic force microscopy (AFM) and scanning tunneling microscopy (STM) can determine the helical angle and handedness of single-wall carbon NTs.[25,26] However, scanning probe methods can only detect a nanoscale region of the outermost surface layer and are not sensitive to the chirality of multi-wall NTs. Practically, AFM and STM measurements are difficult to perform over large areas and for curved surfaces.[27] Liu *et al.* developed a Rayleigh scattering circular dichroism technique that can characterize the chiral indices and handedness of a single-wall carbon NT.[28] This all-optical approach effectively amplifies the weak chiroptical signal by nearly four orders of magnitude, but it requires specialized optical expertise, hardware, and additional sample preparation that suspends a single NT across a micrometer scale slit.

Atomic-resolution TEM imaging has also been employed to determine the chiral handedness of Te nanocrystals[29] and single- and double-walled carbon NTs.[30] Liu *et al.* determined the handedness of double-wall carbon NTs[31] by carefully tilting the NT sample relative to the electron beam, revealing asymmetric lattice fringes that facilitate chirality determination. However, this approach demands that the NT must also be oriented nearly perpendicular to the tilt axes to avoid misassignment. Also, the tilting approach is only reliable for few-walled NTs because multiple walls cause severe fringe overlap. Yu *et al.* developed a method that aligned single-wall carbon NTs with a graphene substrate and used TEM to determine handedness.[32] However, this approach requires depositing samples on a graphene substrate, which can be difficult to fabricate and may not suit all applications where correlated studies on other substrates are preferred.

Before presenting our approach and results, we first illustrate the characterization challenge by reviewing how chiral NT structures are defined and visualized in a TEM. Fig. 1 illustrates how chiral WS_2 NTs form from "rolling" 2D sheets and why their handedness is challenging to determine by TEM imaging alone. Fig. 1a illustrates the case for a left-handed NT that forms by "rolling" the 2D sheet from the dashed blue lines along the direction indicated by the red arrow, producing a left-handed NT with chiral indices $(m, n) = (3, 9)$. Fig. 1b presents a side view of the NT and the black horizontal line indicates a physical division between the upper and lower portions of the NT. Fig. 1c and d show the top-down views of the upper and lower portions of the left-handed NT in Fig. 1a and b, respectively. In a typical TEM imaging experiment of a hollow NT, the experimentalist observes the sum of the top and bottom portions, yielding the pattern shown in Fig. 1e. Fig. 1f–

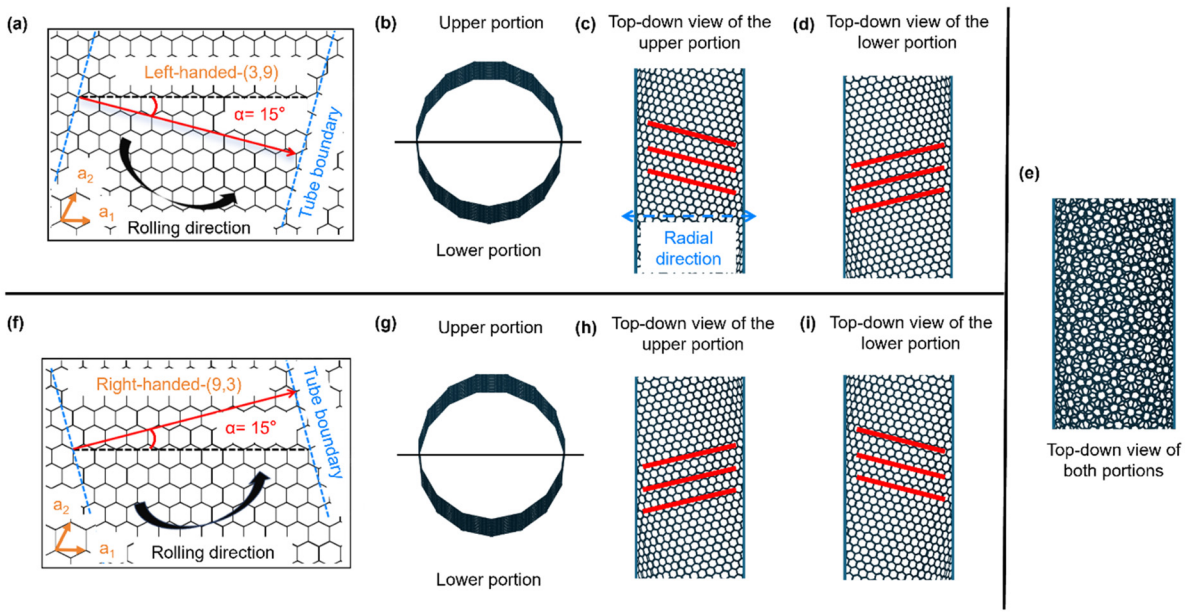

Fig. 1 Cartoon illustration showing how WS_2 NTs form from "rolling" two-dimensional sheets and how the upper and lower portions of a NT appear in a top-down image. (a) Top-down view of a hexagonal lattice where the blue lines indicate the NT boundaries, the dashed black line represents the a_1 lattice direction, and the red arrow represents the lattice vector formed from the chiral indices $(m, n) = (3, 9)$. The chiral angle $\alpha = 15°$ is defined as the angle between the dashed black line and the chiral vector. A chiral NT forms upon rolling the two-dimensional sheet from left to right along the lattice vector (as indicated by the arrow in panel a). (b) Side view of the NT that forms upon rolling the lattice in panel a. The solid black line represents a dividing line between the top and bottom portions of the NT. (c) Top-down view of the top portion of the NT in panel b. (c) Top-down view of the bottom portion of the NT in panel b. (e) Top-down view of the pattern that forms from the sum of the top and bottom portions in panels (c and d). (f–i) The same as panels (a and d), but for a right-handed NT with $(m, n) = (9, 3)$ with the same chiral angle (15°). Importantly, both NTs produce the same pattern (panel e).

i show the analogous process for a right-handed NT with indices (m, n) = (9, 3). Note, the top portion of the right-handed NT shown in Fig. 1h produces the same top-down image as the bottom portion of the left-handed NT in Fig. 1d.[32] The key point is that hollow, right- and left-handed chiral inorganic NTs produce indistinguishable 2D projections (Fig. 1e). Consequently, the absence of a rapid and reliable method for handedness identification has significantly hindered the use of WS_2 NTs in chiral applications.

Another major challenge in determining NT handedness arises from the gap between its formal definition and how samples are viewed and characterized. By definition, right-handed NTs exhibit chiral angles between 0 and 30°, while those of left-handed NTs fall between 30 and 60°.[25,33] This definition, however, assumes that the observer views the NT from a fixed reference orientation. In practice, NTs deposited on substrates may appear rotated, flipped, or inverted, making it unclear whether we are viewing a right- or left-handed NT. The situation is analogous to looking at human hands: a right hand is easily distinguished from a left hand in a person, but in a photograph or mirror image the distinction may become ambiguous.

In this work, we developed an approach to unambiguously identify the handedness of chiral core–shell WO_x–WS_2 NTs using TEM imaging and selected-area electron diffraction (SAED). The oxide core provides a strong lattice contrast that serves as a built-in reference frame for chiral handedness determination, thereby circumventing the sum-image formation problem illustrated in Fig. 1. Importantly, this strategy requires no additional sample preparation. We further show that TEM imaging and SAED yield consistent chiral angles in real and reciprocal space. By overcoming a key bottleneck in handedness determination, this imaging technique enables future fundamental structure–property studies of heterogeneous enantioselective photocatalysis and other emerging chiral applications based on WS_2 nanotubes.

Results and discussion

Fig. 2a shows a top-down TEM image and Fig. 2b shows an edge-on TEM image of an individual multi-walled WS_2 NT surrounding a tungsten oxide-based core. The red lines in Fig. 2a indicate the presence of eight continuous WS_2 layers. A distinct contrast variation appears at the core/shell interface. The oxide core exhibits a periodic stripe-like lattice contrast, indicating crystallinity (Fig. 2a-inset), and is assigned to $W_{18}O_{49}$ based on prior reports for this system.[34] The $W_{18}O_{49}$ core shows lattice fringes with a spacing of 0.38 nm (d(010)), whereas the WS_2 shell shows fringes of 0.25 nm (Fig. S1), consistent with d(100) of WS_2.[18,35] In addition to the distinct 0.63 nm d-spacing between WS_2 layers creating the NT wall, corresponding to the (002) direction, the layers are oriented at a clear angle relative to the nanotube axis. This contrasts with the monoclinic $W_{18}O_{49}$ core, which grows along the [010] direction (b-axis) approximately perpendicular to the tube axis. The distinct fringe orientation further confirms that the observed 0.25 nm spacing arises from the WS_2 shell rather than the oxide core. The NT appearance in Fig. 2a suggests a cylindrical morphology; however, the NT exhibits a prismatic cross-section with polygonal faces (Fig. 2b). For this reason, the WS_2 layers on the right and left sides of the NT in Fig. 2a do not produce similar contrast in TEM images.

Despite the oxide core dominating the TEM contrast (white box, Fig. 2a), lattice fringes from the upper WS_2 layers remain clearly visible in many high-resolution TEM images. Fig. 3 shows representative images where lattice fringes from both WS_2 and WO_x are clearly visible. The lattice fringes of WS_2

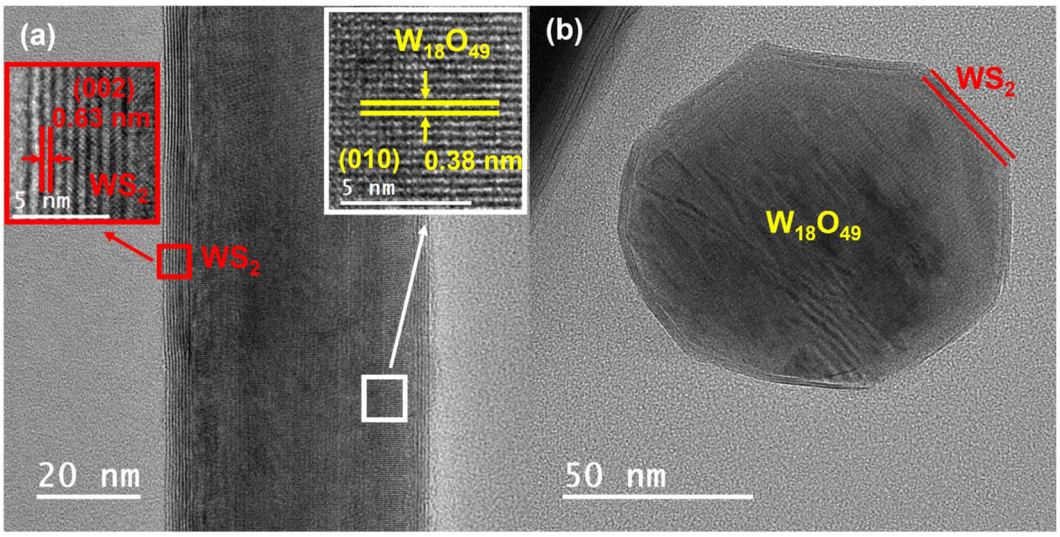

Fig. 2 (a) TEM image of an eight-layer-thick core–shell WO_x–WS_2 NT viewed along the longitudinal axis; the left inset shows a zoomed-in view of the WS_2 interlayer (002) lattice spacing of 0.63 nm indicated by the red box. The right inset shows a zoomed-in view of the oxide/shell interface indicated by the white box. The yellow lines display the (010) lattice spacing of 0.38 nm. (b) TEM image of a different four-layer core–shell WO_x–WS_2 NT viewed along the axial axis. The red lines indicate the WS_2 lattice orientation.

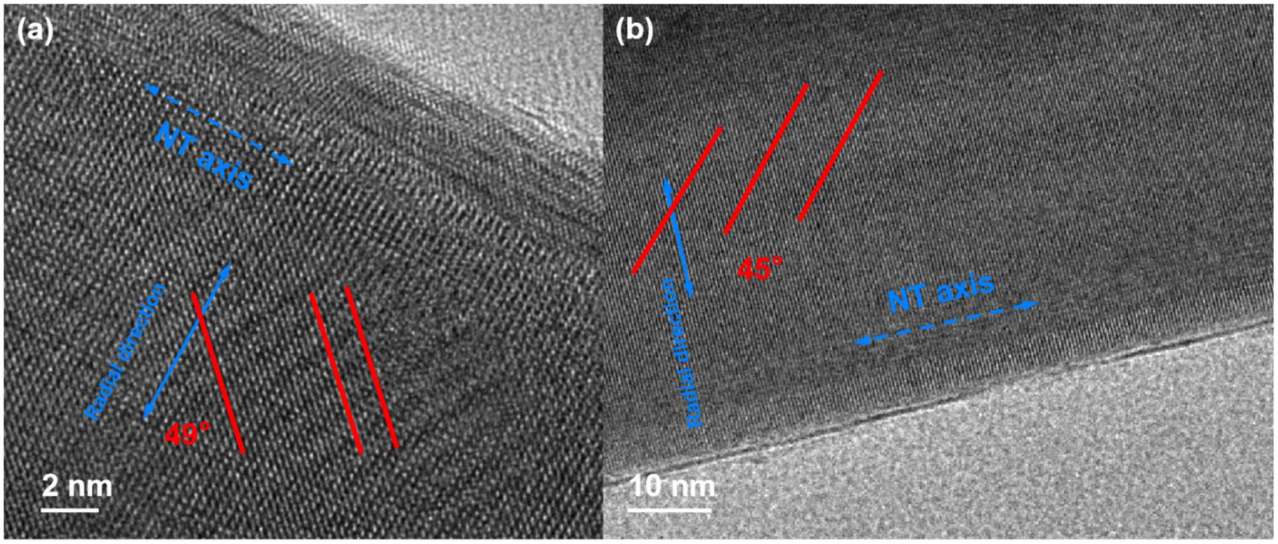

Fig. 3 TEM images of WO_x/WS_2 NTs where the WS_2 lattice fringes are oriented (a) 49° and (b) 45° relative to the radial direction of the NT (blue lines).

likely stem from the upper WS_2 layers because any contribution from the lower WS_2 layers is strongly attenuated by the oxide core (see Fig. 1c and d for an illustration of the top and bottom NT views and TEM projections). As the electron beam enters the nanotube from the top, the upper WS_2 layers are the first region where the electron wave can interact coherently with the atoms in the material, generating lattice-fringe phase contrast. After propagating through the thick oxide core, strong inelastic scattering associated with the high atomic number of tungsten is expected to reduce the coherence of the electron wave, thereby attenuating any lattice-fringe contribution from the lower WS_2 layers. We developed a step-by-step procedure, described and illustrated in Fig. S1 and S2 of the SI, to confirm that the lattice fringes in Fig. 3 stem from the WS_2 layers in addition to WO_x. Briefly, the procedure consists of generating an FFT from a selected area of the TEM image, selecting the FFT spots associated with the WS_2 lattice, and applying an inverse FFT to those spots alone to reconstruct a real-space image that reveals the WS_2 lattice-fringe orientation.

Before we introduce our approach to determine the handedness of inorganic NTs using real space TEM imaging, we briefly review how to determine the chiral angle of a single NT using SAED. Fig. 4 schematically shows the SAED analysis procedure for a three-layer thick chiral WS_2 NT. The chiral angles from SAED patterns are calculated using $D_1 = D_2 + D_3$,[33] where D_1, D_2, and D_3 represent the distances between the equatorial line and the first, second, and third diffraction lines of WS_2, respectively (from the top toward the equatorial line). The equatorial line corresponds to the diffraction from lattice planes that are perpendicular to the NT axis. Each WS_2 layer produces a diffraction line and, therefore, the number of diffraction lines correlates with the number of WS_2 layers. In Fig. 4, a three-layer-thick NT produces diffraction features (arising from the hexagonal lattice) composed of three streaks.

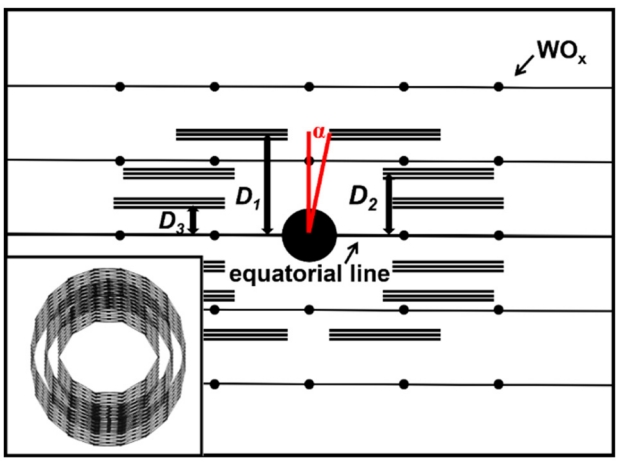

Fig. 4 Cartoon illustration of an idealized SAED pattern of a three layer-thick chiral core–shell WO_x–WS_2 NT. D_1, D_2, and D_3 represent the distances between the equatorial line and the first, second, and third diffraction lines of WS_2, respectively (from the top toward the equatorial line). The angle α indicates the chiral angle. The black dots represent WO_x reflections. The inset shows the corresponding simulated three-layer WS_2 NT structure.

These streaks correspond to diffraction from the three concentric layers of the NT wall. Within each set, the streak farthest from the center originates from the innermost layer with the smallest diameter, while the streak closest to the center arises from the outermost layer with the largest diameter.

The chiral angle α is calculated using:

$$\alpha = \tan^{-1}\left(\frac{2D_2 - D_1}{\sqrt{3}\,D_1}\right) = \tan^{-1}\left(\frac{D_1 - 2D_3}{\sqrt{3}\,D_1}\right) = \tan^{-1}\left(\frac{D_2 - D_3}{\sqrt{3}\,(D_2 + D_3)}\right)$$

All layers of a multilayer WS_2 NT typically share the same handedness, differing only by a few degrees, and the measured angles can be assigned to individual layers in sequence.[33,36] Therefore, the average angle is taken in the SAED pattern by using the midpoint of each diffraction line to represent the average angle of this NT, as described in Fig. S3. Following the approach by Deniz and Qin who showed that each layer in a multiwall WS_2 NT adopts similar chiral structures,[36] we assume that each layer of a multiwalled NT shares the same handedness. The rationale for this assumption and the consequences of chiral angle averaging are discussed in the Results and discussion section.

Having discussed how to determine the chiral angle *via* SAED, we now show how the unique TEM image contrast produced by the upper WS_2 layers can be used to determine the right- or left-handedness of a single NT, which cannot be done for hollow WS_2 NTs. Fig. 5a shows low- and high-resolution TEM images of a 2-layer thick WO_x–WS_2 NT. The critical angle observed *via* SAED is 16° (Fig. 5a, top right inset). However, the SAED-derived angle does not reveal the chiral handedness directly. Fig. 5b and c show the possible lattice orientations for right- and left-handed NTs with 60° symmetry and the same SAED-derived chiral angle of 16°. Next, we compare the lattice fringes determined *via* TEM imaging (Fig. 5a, bottom right inset) to the two possible configurations in Fig. 5b and c. For this NT, we observe WS_2 lattice fringes oriented 46° relative to the NT radial direction, as indicated by the red lines in the bottom right inset of Fig. 5a. The right-handed NT configuration shown in Fig. 5b illustrates a right-handed chiral inorganic NT where the lattice orientation of the WS_2 lattice fringes would be oriented 44° relative to the NT radial direction, which is 2° less than the 46° angle measured in real space TEM images. The small 2° difference between the SAED- and TEM-derived angles (44° *versus* 46°, respectively) is likely

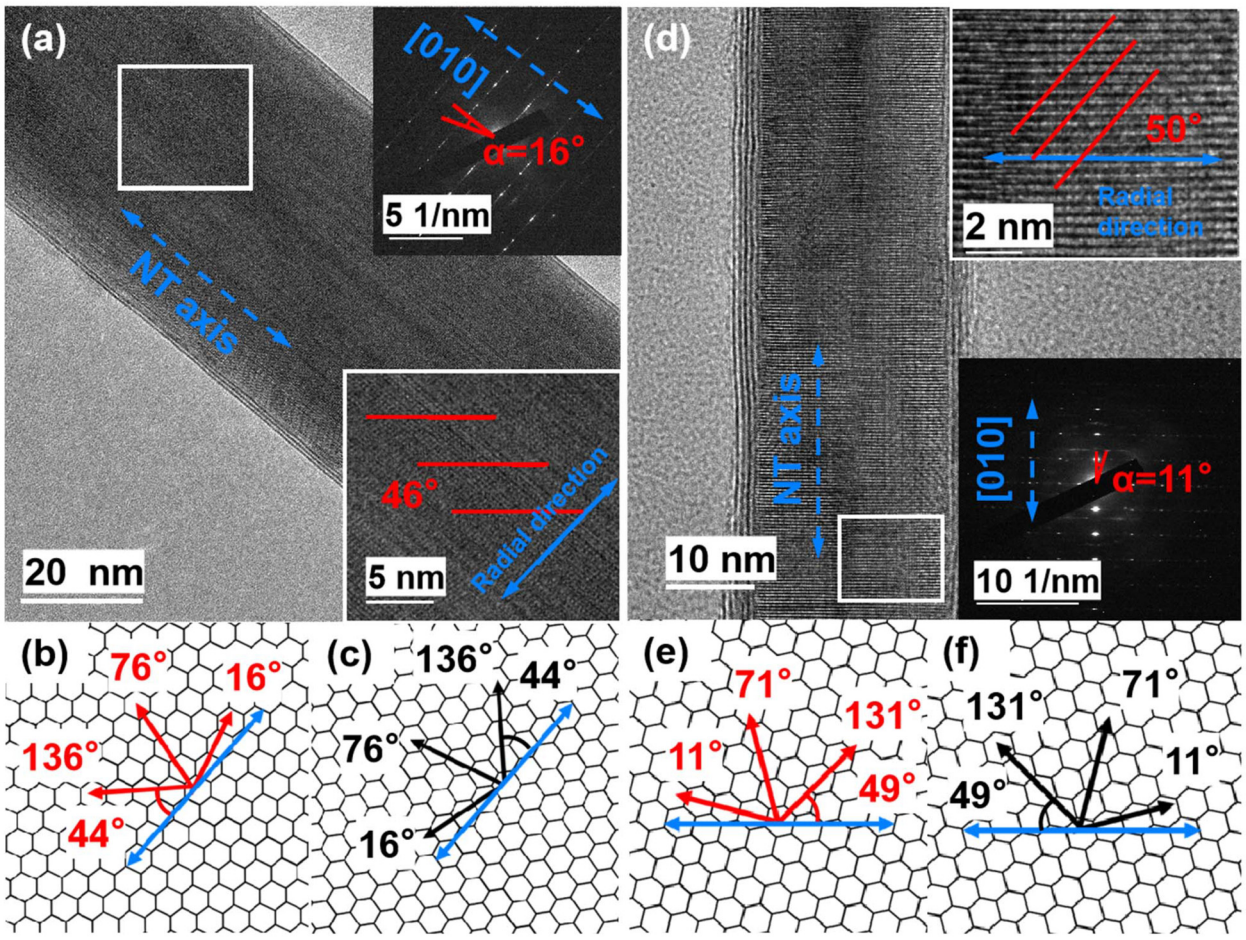

Fig. 5 Two examples showing the consistency of chiral angles measured by TEM and SAED. (a) TEM image of a right-handed two-layer-thick WS_2 NT. The top right inset shows the SAED pattern and the chiral angle determined from SAED analysis. The bottom right inset shows a zoomed-in view from the white box region in panel a. The blue arrow indicates the radial direction of the NT and the red lines represent the WS_2 lattice. The [010] direction is displayed by a blue arrow in the SAED inset. (b and c) The reference frame of panel a that relates the right-handed (b, red) and left-handed (c, black) TEM-derived angle (46°) to the chiral angle measured *via* SAED (16°). (d–f) Same as panels a–c, but for a left-handed four-layer-thick WS_2 NT. In panels b, c and e, f, red frames indicate the WS_2 lattice orientation corresponding to the correct handedness assignment, whereas black frames indicate the incorrect handedness for comparison.

due to the fact that it is difficult to determine which layer in the multi-layer wall structure contributes to the contrast in TEM imaging; SAED, in principle, is able to distinguish each chiral layer from each layer (see Fig. 4). The key point of Fig. 5a–c is that the 46° angle obtained from real-space imaging relates to the SAED-determined angle of 16° *via* 60° symmetry, revealing the handedness of a single NT.

Fig. 5d–f further illustrate the consistency between real space TEM imaging and SAED for a left-handed, four-layer thick NT. In this case, the SAED-derived angle is 11° (Fig. 5d, bottom right inset). Fig. 5e and f show two possible WS_2 lattice orientations with the chiral angle of 11°. High-resolution TEM imaging reveals a 50° angle between the WS_2 lattice and the radial NT direction (Fig. 5d, top right inset). Following the symmetry argument discussed above, one can see how the SAED angle of 11° corresponds to a TEM-determined value of 50° for the left-handed configuration in Fig. 5e. Another right-handed example is shown in Fig. S4 and S5.

In some cases, moiré patterns appear in the TEM images of core–shell NTs, providing another direct and straightforward way to define the chiral handedness. The presence of the moiré patterns in our samples was validated by high-angle annular dark-field scanning transmission electron microscopy (HAADF-STEM) imaging (Fig. S6). Fig. 6 shows NTs with moiré patterns that arise from the superposition of the WS_2 lattice and the WO_x core lattice. The stripe-like lattice of tungsten oxide readily produces moiré patterns. These stripe-like patterns are distinct from the WS_2 lattice. We distinguish the WO_x lattice from the WS_2 lattice by its alternating contrast and its larger periodic spacing compared to WS_2, as shown in Fig. 6.

Fig. 6a illustrates a representative case for determining chiral handedness using moiré patterns formed between the WO_x core and WS_2 layers. Fig. 6a top left inset shows a distinct moiré pattern with a 34° left-orientation relative to the NT radial direction, whereas the WS_2 lattice exhibits a 49° right orientation. SAED analyses yield an average chiral angle of 9° (Fig. S7a), which can be rationalized using the reference frame in Fig. 6b. Hence, the NT in Fig. 6a is left-handed with an 11° chiral angle. Simulations of a 49° right-oriented WS_2 NT and a WO_x core in Fig. 6a (bottom right inset) predict the opposite orienting relationship between the moiré pattern and WS_2 lattice: the overlap between the hexagonal WS_2 lattice points and the WO_x rectangular points. The simulated moiré pattern exhibits a 43° angle relative to the radial direction (Fig. 6a-inset). We note the inconsistency between the TEM-derived angle and that of the simulated moiré pattern; a small misalignment or space difference results in a large change in the moiré pattern angle.[37] It is also possible that the multiwall structure contributes to the error between the TEM-derived value and SAED,[38] as discussed above.

The single-walled NT in Fig. 6d shows a 66° moiré pattern, but oriented in a different direction relative to the NT radial direction as in Fig. 6a. A zoomed-in view confirms that the WS_2 lattice is oriented 45° relative to the NT radial direction. This corresponds to a 15° chiral angle, which can be rationalized using the reference frame in Fig. 6c, closely matching the SAED-derived 14° angle (Fig. S7b). The accompanying simulation in the Fig. 6d-inset shows a 45°-rotated WS_2 lattice superimposed on the line-like tungsten oxide lattice, producing a moiré pattern with a 66° angle, consistent with the TEM observations.

In all cases, we observed good agreement (<2°) between TEM-derived and SAED-derived chiral angles (Table 1 and Fig. S8). The slight disagreement between TEM- and SAED-derived chiral angles is likely due to the manual image analysis procedure. There is a critical need to develop automated and robust image

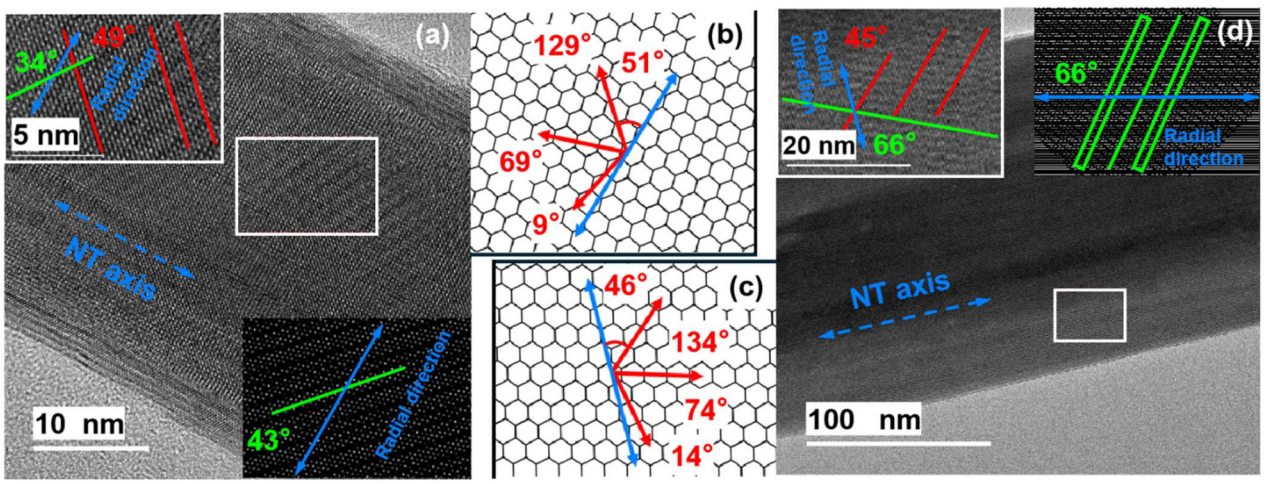

Fig. 6 Utilizing moiré patterns for chiral handedness identification. (a) TEM image of a left-handed 5-layer multi-walled WS_2 NT with a visible stripe-like moiré pattern. Top left inset shows a zoomed-in view of the moiré pattern from the white boxed region in panel a. In the top left inset panel, the red and green lines represent the WS_2 lattice and moiré pattern, respectively. The 49° and 34° represent the angles formed by the WS_2 lattice and the moiré pattern relative to the radial direction, which is represented with a blue double-sided arrow. The bottom right inset shows the moiré pattern simulation. (b) Cartoon illustration of the reference frames depicting the chiral angles and the orientation of the WS_2 lattice relative to the NT radial direction for the NTs in panel a. (c and d) Same as panels a and b, but for a right-handed single-walled WS_2 NT.

Table 1 Comparison of chiral angles determined by TEM and SAED, their differences, and corresponding handedness assignments for WS_2 NTs

Number	Chiral angle (TEM)	Chiral angle (SAED)	Difference	Handedness
1	11°	9°	2°	Left
2	15°	14°	1°	Right
3	12°	14°	2°	Right
4	10°	11°	1°	Left
5	14°	16°	2°	Left
6	6°	5°	1°	Left
7	16°	16°	0°	Left
8	16°	16°	0°	Left
9	14°	14°	0°	Right

analysis procedures that leverage data and simulations to define the chiral angle and handedness, which is beyond the scope of this work. However, the close agreement between TEM and SAED values demonstrates the repeatability and reliability of the proposed method despite the fact that multi-shelled NTs inherently exhibit a few degrees of variation in chiral angles among each layer.[33] The methods proposed herein can be extended to other core–shell NT materials (MoS_2 NTs,[2,39,40] BN NTs,[41] and carbon NTs[42,43]), where the core material provides a reference frame contrast for the chiral shell material.

Conclusions

In summary, we established a rapid, straightforward TEM approach for determining the handedness of core–shell WO_x-WS_2 NTs. The method leverages the strong contrast of the WO_x core, which effectively masks the lower WS_2 layers, allowing the handedness of the exposed upper layers to be identified in real-space TEM projections. In this work, we demonstrate this workflow for nanotube diameters of 25–200 nm with WS_2 shells comprising 1–5 layers. In general, increasing WS_2 shell thickness and/or overall tube diameter is expected to reduce the visibility of the top-layer WS_2 fringes in projection, and thin WO_x cores may limit the ability to suppress contributions from the lower portion of the nanotube. The results were validated using SAED analysis and structural simulation. In some cases, analysis of WO_x–WS_2 moiré patterns provides additional verification. This strategy requires no specialized sample preparation and is broadly accessible in any high-resolution TEM. Beyond core–shell WO_x–WS_2, the principle of disentangling overlapping structural signals can be extended to other chiral nanostructures, enabling more reliable handedness assignment and opening opportunities for chirality-dependent applications of inorganic nanotubes.

Methods

NT synthesis

Core–shell WO_x–WS_2 NTs were synthesized in a horizontal reactor by sulfurization of the $W_{18}O_{49}$ nanowhiskers, as described previously.[19,34]

TEM sample preparation and characterization

The NTs were dispersed in anhydrous ethanol (200 proof), sonicated for 30 seconds in a sonicator (VWR 97044-002), and 5 μL of the solution was drop-cast onto a carbon-coated Cu TEM grid. After drop-casting, the TEM grids were dried in air for 2 h before imaging. High-resolution TEM imaging and SAED experiments were conducted on a JEOL JEM-2100F electron microscope operated at 200 kV. Images were acquired with a Gatan Ultrascan CCD camera using an acquisition time of 1–6 s. Image and SAED diffraction data were processed using Digital Micrograph software (v3.61).

Author contributions

Kaiyuan Wang: conceptualization, formal analysis, methodology, investigation, resources, data curation, validation, visualization, and original draft writing, review and editing. Beilynn Geiss: formal analysis, investigation, validation, methodology, and original draft writing, review and editing. Roy Geiss: methodology, data curation, formal analysis, investigation, validation, original draft writing, review and editing. James R. Neilson: supervision, formal analysis, and review. Alla Zak: supervision, synthesis of nanotubes, formal analysis, and review. Justin B. Sambur: conceptualization, methodology, data curation, original draft writing, review and editing, project administration, and funding acquisition.

Conflicts of interest

There are no conflicts to declare.

Data availability

All data generated or analysed in this study are included in this article and the supplementary information (SI). The SI contains supporting information on the TEM analysis procedure, TEM images showing lattice spacings, analyses of additional samples, a HAADF-STEM image, and the TEM–SAED analysis procedure. See DOI: https://doi.org/10.1039/d6nr00074f.

Acknowledgements

This work was supported by the donors of ACS Petroleum Research Fund under New Directions Grant 66052-ND10 and the National Science Foundation (DMR-2046948). A. Z. acknowledges support from the Ministry of Innovation, Science & Technology grants # 0006701 and #0007244, Israel.

References

1 R. Tenne and M. Redlich, *Chem. Soc. Rev.*, 2010, **39**, 1423–1434.

2 F. Qin, W. Shi, T. Ideue, M. Yoshida, A. Zak, R. Tenne, T. Kikitsu, D. Inoue, D. Hashizume and Y. Iwasa, *Nat. Commun.*, 2017, **8**, 14465.
3 S. Dey, K. Manjunath, A. Zak and G. Singh, *ACS Omega*, 2023, **8**, 10126–10138.
4 J. Lin, Z. Hu, H. Li, J. Qu, M. Zhang, W. Liang and S. Hu, *Inorg. Chem.*, 2019, **58**, 9833–9843.
5 M.-C. Pignié, V. Shcherbakov, T. Charpentier, M. Moskura, C. Carteret, S. Denisov, M. Mostafavi, A. Thill and S. Le Caër, *Nanoscale*, 2021, **13**, 3092–3105.
6 A. Laikhtman, S. Michaelson, A. Hoffman, T. K. Kim, H. R. Moon and A. Zak, *Int. J. Hydrogen Energy*, 2014, **39**, 9837–9841.
7 J. L. Musfeldt, Y. Iwasa and R. Tenne, *Phys. Today*, 2020, **73**, 42–48.
8 M. Wilson, *Chem. Phys. Lett.*, 2004, **397**, 340–343.
9 L. Kachtík, D. Citterberg, K. Bukvišová, L. Kejík, F. Ligmajer, M. Kovařík, T. Musálek, M. Krishnappa, T. Šikola and M. Kolíbal, *Nano Lett.*, 2023, **23**, 6010–6017.
10 Y. Yan, M. Shaikh, M. C. Beard, J. Gu and I. Hendrix, *Sci. Adv.*, 2025, eadw5850.
11 Y. Sang, F. Tassinari, K. Santra, W. Zhang, C. Fontanesi, B. P. Bloom, D. H. Waldeck, J. Fransson and R. Naaman, *Proc. Natl. Acad. Sci. U. S. A.*, 2022, **119**, e2202650119.
12 B. P. Bloom, Y. Lu, T. Metzger, S. Yochelis, Y. Paltiel, C. Fontanesi, S. Mishra, F. Tassinari, R. Naaman and D. H. Waldeck, *Phys. Chem. Chem. Phys.*, 2020, **22**, 21570–21582.
13 T. S. Metzger, S. Mishra, B. P. Bloom, N. Goren, A. Neubauer, G. Shmul, J. Wei, S. Yochelis, F. Tassinari, C. Fontanesi, D. H. Waldeck, Y. Paltiel and R. Naaman, *Angew. Chem., Int. Ed.*, 2020, **59**, 1653–1658.
14 Y. X. Foo, A. Kermiche, F. T. Chowdhury, C. D. Aiello and L. D. Smith, *Chem. Phys. Rev.*, 2025, **6**, 031306.
15 Y. Dong, M. P. Hautzinger, M. A. Haque and M. C. Beard, *Annu. Rev. Phys. Chem.*, 2025, **76**, 519–537.
16 P. Chithaiah, S. Ghosh, A. Idelevich, L. Rovinsky, T. Livneh and A. Zak, *ACS Nano*, 2020, **14**, 3004–3016.
17 A. Zak, L. Sallacan-Ecker, A. Margolin, Y. Feldman, R. Popovitz-Biro, A. Albu-Yaron, M. Genut and R. Tenne, *Fullerenes, Nanotubes Carbon Nanostruct.*, 2010, **19**, 18–26.
18 Z. Liu, A. W. A. Murphy, C. Kuppe, D. C. Hooper, V. K. Valev and A. Ilie, *ACS Nano*, 2019, **13**, 3896–3909.
19 V. Kundrát, L. Novák, K. Bukvišová, J. Zálešák, E. Kolíbalová, R. Rosentsveig, M. B. Sreedhara, H. Shalom, L. Yadgarov, A. Zak, M. Kolíbal and R. Tenne, *ACS Nano*, 2024, **18**, 12284–12294.
20 B. Seo, H. Y. Jeong, S. Y. Hong, A. Zak and S. H. Joo, *Chem. Commun.*, 2015, **51**, 8334–8337.
21 Z. Dong and Y. Ma, *Nat. Commun.*, 2020, **11**, 1588.
22 L.-C. Qin, *Rep. Prog. Phys.*, 2006, **69**, 2761–2821.
23 H. Deniz, A. Derbakova and L.-C. Qin, *Ultramicroscopy*, 2010, **111**, 66–72.
24 Z. Liu and L.-C. Qin, *Chem. Phys. Lett.*, 2005, **405**, 265–269.
25 Y. Chen, Z. Shen, Z. Xu, Y. Hu, H. Xu, S. Wang, X. Guo, Y. Zhang, L. Peng, F. Ding, Z. Liu and J. Zhang, *Nat. Commun.*, 2013, **4**, 2205.
26 T. W. Odom, J.-L. Huang, P. Kim and C. M. Lieber, *Nature*, 1998, **391**, 62–64.
27 J. Shen, D. Zhang, F.-H. Zhang and Y. Gan, *Appl. Surf. Sci.*, 2017, **422**, 482–491.
28 F. Yao, W. Yu, C. Liu, Y. Su, Y. You, H. Ma, R. Qiao, C. Wu, C. Ma, P. Gao, F. Xiao, J. Zhao, X. Bai, Z. Sun, S. Maruyama, F. Wang, J. Zhang and K. Liu, *Nat. Nanotechnol.*, 2021, **16**, 1073–1078.
29 J. Hu, Z. Dong, C. Chu and Y. Ma, *Nat. Chem.*, 2025, **17**, 1819–1825.
30 A. W. Robertson and J. H. Warner, *Nanoscale*, 2013, **5**, 4079.
31 Z. Liu, K. Suenaga, H. Yoshida, T. Sugai, H. Shinohara and S. Iijima, *Phys. Rev. Lett.*, 2005, **95**, 187406.
32 Y. Yu, Y. Zhao, S. Li, C. Zhao, W. Liu, S. Wang, F. Ding and J. Zhang, *Adv. Sci.*, 2023, **10**, 2206403.
33 Y. Chen, H. Deniz and L.-C. Qin, *Nanoscale*, 2017, **9**, 7124–7134.
34 A. Zak, L. Sallacan-Ecker, A. Margolin, M. Genut and R. Tenne, *NANO*, 2009, **04**, 91–98.
35 Y. Chen, Y. Li, Y. Wang, T. Tian and L.-C. Qin, *Mater. Res. Lett.*, 2017, **5**, 508–515.
36 H. Deniz and L.-C. Qin, *Chem. Phys. Lett.*, 2012, **552**, 92–96.
37 G. Oster and Y. Nishijima, *Sci. Am.*, 1963, **208**, 54–63.
38 M. B. Sadan, L. Houben, A. N. Enyashin, G. Seifert and R. Tenne, *Proc. Natl. Acad. Sci. U. S. A.*, 2008, **105**, 15643–15648.
39 S. S. Sinha, L. Yadgarov, S. B. Aliev, Y. Feldman, I. Pinkas, P. Chithaiah, S. Ghosh, A. Idelevich, A. Zak and R. Tenne, *J. Phys. Chem. C*, 2021, **125**, 6324–6340.
40 P. Chithaiah, S. Ghosh, A. Idelevich, L. Rovinsky, T. Livneh and A. Zak, *ACS Nano*, 2020, **14**, 3004–3016.
41 Y. Nakanishi, S. Furusawa, Y. Sato, T. Tanaka, Y. Yomogida, K. Yanagi, W. Zhang, H. Nakajo, S. Aoki, T. Kato, K. Suenaga and Y. Miyata, *Adv. Mater.*, 2023, **35**, 2306631.
42 N. Kanda, Y. Nakanishi, D. Liu, Z. Liu, T. Inoue, Y. Miyata, D. Tománek and H. Shinohara, *Nanoscale*, 2020, **12**, 17185–17190.
43 I. Çaha, A. U. Ahmad, L. Boddapatti, M. Bañobre-López, A. T. Costa, A. N. Enyashin, W. Li, P. Gargiani, M. Valvidares, J. Fernández-Rossier and F. L. Deepak, *Commun. Chem.*, 2025, **8**, 155.

